Crater Edge-based Flexible Autonomous Navigation for Planetary Landing

Yang Tian[1], Meng Yu[2], Meibao Yao[1] and Xiangyu Huang[3]

[1](*Harbin Institute of Technology, School of Astronautics*)
[2](*Nanjing University of Aeronautics and Astronautics, School of Astronautics*)
[3](*Chinese Academy of Space Technology*)
(E-mail: yuxy21@nuaa.edu.cn)

In this paper, a novel method for autonomous navigation for an extra-terrestrial body landing mission is proposed. Based on state-of-the-art crater detection and matching algorithms, a crater edge-based navigation method is formulated, in which solar illumination direction is adopted as a complementary optical cue to aid crater edge-based navigation when only one crater is available. To improve the pose estimation accuracy, a distributed Extended Kalman Filter (EKF) is developed to encapsulate the crater edge-based estimation approach. Finally, the effectiveness of proposed approach is validated by Monte Carlo simulations using a specifically designed planetary landing simulation toolbox.

1. INTRODUCTION.   Autonomous landing on an extra-terrestrial body has become one of the key technologies for future space missions. By employing an autonomous pin-point landing technology, a planetary exploration mission will obtain more scientific exploration rewards in a safe manner. To achieve a safe landing, the relative pose of a lander with respect to the pre-determined landing spot must be updated in real-time. Inertial navigation solutions are technically ready for implementation on board landers but cannot meet the requirement for relative state updates. To this end, many studies have proposed to introduce Terrain Relative Navigation (TRN) technology to compensate the inertial navigation. In 2005, the *Hayabusa* probe utilised several Ground Control Points (GCP) to carry out relative pose estimation, and successfully carried out two touchdowns on a small extra-terrestrial body, named Itokawa (Terui et al., 2010). For the Mars Exploration Rover (MER) mission, a TRN method named Descent Image Motion Estimation System (DIMES) was developed (Cheng et al., 2005). This enabled real-time estimation of the horizontal velocity of the Mars lander. The Origins SPECtral Interpretation Resource Identification Security Regolith Explorer (OSIRIS-REx) carried an autonomous navigation system, in which a Three-Dimensional (3D) asteroid terrain model was introduced as a navigation map to carry out TRN (Berry et al., 2013; Lorenz et al., 2017). This is similar to the approach

used in the *Rosetta* mission for comet rendezvous and lander delivery operations (Pardo de Santayana and Lauer, 2015).

A typical TRN method relies on sensing several pre-mapped terrain landmarks to estimate the relative pose. One reliable navigation TRN landmark for such a mission is a crater (Johnson and Montgomery et al., 2008). A crater usually possesses a fixed parabolic or truncated cone shape and appears as a circular or elliptical outline in a descent image. Compared to other terrain landmarks, craters have more salient and stable features, thus many studies have proposed to use craters to carry out TRN in missions to the Moon and for small body orbiting and landing. Briefly, craters are first detected from descent images, and then matched to a crater database to estimate the relative position. In representative studies proposed by Cheng et al. (2003) and Leroy et al. (2001), the Canny Edge Detector (Canny, 1986) is employed to detect salient edges from a descent image. After that, edges that belong to the same crater are grouped into a closed ellipse by referring to grey-scale gradients or curvatures. Another type of crater detection method is based on image region segmentation (Spigai et al., 2010; Singh and Lim, 2008; Yu et al., 2014). The main idea is to extract the bright and shadow areas inside a crater and formulate affine-invariant features. Other methods include using an image template (Bandeira et al., 2007) or Hough Transform (Johnson, 2000) to detect craters. A milestone study of crater matching is the algorithm proposed by Cheng et al. (2003), in which affine invariants are extracted from representative fitting ellipses, and then casted as vectors to realise crater matching. After crater detection and matching, centres of matched craters are used as navigational landmarks. These can also be fused with inertial measurements as claimed by Singh and Lim (2008), Cheng and Ansar (2005), Simard Bilodeau et al. (2012) and Rohrschneider (2011) to improve the performance of relative state estimation.

To cope with the landing scenario where the number of craters is insufficient for navigation, many studies have also proposed using general image features (Ansar, 2004; Johnson and SanMartin, 2000; Johnson et al., 2007). A general feature matching method might suffer from scale and rotation differences between descent images and navigation maps. To improve feature matching performance, some studies have proposed to first project the descent image onto the navigation map by referring to the current pose estimation, and then carry out feature matching (Cheng et al., 2005; Johnson et al., 2015; Mourikis et al., 2009). A similar approach is to render a reference terrain map based on current pose estimation and a three-dimensional model of the target landing spot (Lorenz et al., 2017; Pardo de Santayana and Lauer, 2015; Gaskell, 2001; Montgomery et al., 2006), in which feature matching is carried out between descent images and the rendered map. Under this manner, the reference map and the descent image are similar in the affine-scale, leading to more accurate feature matching, but at the expense of higher computational costs.

Most of the existing crater-based navigation research has employed the centre of a crater as the landmark. However, when the optical axis of the on board camera is not parallel to the planar normal of the crater's outer rim, the line-of-sight from a crater's centre in a descent image will deviate from the ground truth, which inevitably results in errors in relative position estimation. Moreover, solely utilising line-of-sight of the crater's centre as a navigational observation does not make full use of the optical information from a crater. For this reason, this paper develops a novel crater edge-based navigation solution, and formulates a complete crater-based navigation solution, in which crater edges are employed under a distributed Extended Kalman Filter (EKF). In addition, solar illumination direction is introduced to aid crater edge-based navigation when only one crater is available for

navigation. Simulation results have verified that the new approach performs better than current state-of-the-art crater centre-driven navigation solutions.

The rest of this paper is organised as follows: Section 2 formulates the problem; Section 3 introduces the crater edge-based navigation method; Section 4 presents Monte Carlo simulations and discussion and conclusions are drawn in Section 5.

2. PROBLEM FORMULATION.   The camera's observation model utilises a traditional pin-hole transformation model, such that:

$$
\begin{aligned}
u_0 &= fx_c/z_c \\
v_0 &= fy_c/z_c
\end{aligned}
\tag{1}
$$

where (x_c, y_c, z_c) are the 3D coordinates of a feature on the planetary terrain, (u_0, v_0) are the coordinates of the corresponding pixels in the image plane and f is the focal length of the on board camera. If a crater is detected in a descent image, its edges will satisfy the general equation of an elliptical curve:

$$
Au^2 + Buv + Cv^2 + Du + Ev + F = 0
\tag{2}
$$

The elliptical curve equation can also be organised into a quadratic form:

$$
[u \ v \ 1]
\begin{bmatrix}
A & B/2 & D/2 \\
B/2 & C & E/2 \\
D/2 & E/2 & F
\end{bmatrix}
\begin{bmatrix}
u \\
v \\
1
\end{bmatrix}
= [u \ v \ 1]Q
\begin{bmatrix}
u \\
v \\
1
\end{bmatrix}
= 0
\tag{3}
$$

where $u = u_0/f$ and $v = v_0/f$. According to the characteristics of the elliptical curve equation, the centre of the crater edge in the image frame is:

$$
X_0 = f \left[\frac{2CD - BE}{B^2 - 4AC} \quad \frac{2AE - BD}{B^2 - 4AC} \quad 1 \right]^T
\tag{4}
$$

Denote by $X_c = [x_c, y_c, z_c]^T$ a point that is located on a conic surface intersecting with the crater edge in the image frame. Equation (3) can thus be expressed by:

$$
X_c^T Q X_c = 0
\tag{5}
$$

Denote by $n_c = [n_x \ n_y \ n_z]^T$ a normal vector of the plane the crater edge lies in, thus:

$$
n_c^T X_c = d
\tag{6}
$$

where d is the distance between the crater edge plane and the optical centre of the camera. An actual 3D crater edge should satisfy Equations (5) and (6) at the same time. According to Equation (6), z_c can be obtained such that $z_c = (d - n_x x_c - n_y c_y)/n_z$. Substituting z_c into Equation (5), the coordinates of the X-axis and Y-axis of the crater edge points can be expressed by:

$$
[x_c \quad y_c \quad 1]
\begin{bmatrix}
A' & B'/2 & D'/2 \\
B'/2 & C' & E'/2 \\
D'/2 & E'/2 & F'
\end{bmatrix}
\begin{bmatrix}
x_c \\
y_c \\
1
\end{bmatrix}
= [x_c \quad y_c \quad 1]Q'
\begin{bmatrix}
x_c \\
y_c \\
1
\end{bmatrix}
= 0
\tag{7}
$$

where $A' = n_z^2 A - n_x n_z D + n_x^2 F$, $B' = n_z^2 B - n_y n_z D - n_x n_z E + 2n_x n_y F$, $C' = n_z^2 C - n_y n_z E + n_y^2 F$, $D' = dn_z D - 2dn_x F$, $E' = dn_z E - 2dn_y F$ and $F' = d^2 F$.
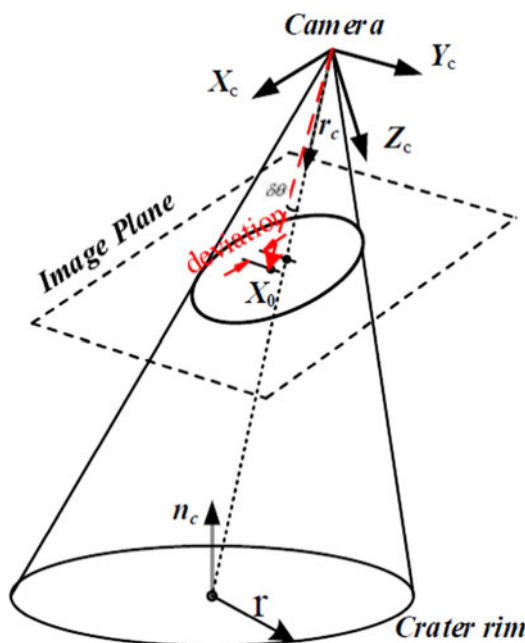
Figure 1.   Illustration of deviation between line-of-sight of crater centre in a descent image and that of its counterpart in the crater map.

Following Equation (6) and utilising the elliptical curve property, the line of sight direction of the crater centre can be obtained:

$$r_c = \left[\begin{array}{ccc} \dfrac{n_z k_1 + n_x k_4 + n_y k_5}{n_z k_3 + n_x k_1 + n_y k_2} & \dfrac{n_z k_2 + n_x k_5 + n_y k_6}{n_z k_3 + n_x k_1 + n_y k_2} & 1 \end{array}\right]^T \qquad (8)$$

Or equally:

$$r_c = [n_x k_4 + n_y k_5 + n_z k_1 \quad n_x k_5 + n_y k_6 + n_z k_2 \quad n_x k_1 + n_y k_2 + n_z k_3]^T \qquad (9)$$

where $k = 2CD - BE$, $k_2 = 2AE - BD$, $k_3 = B^2 - 4AC$, $k_4 = E^2 - 4CF$, $k_5 = 2BF - DE$ and $k_6 = D^2 - 4AF$.

According to Equations (8) and (4), when $n_x = 0$ and $n_y = 0$, the normal of the plane where the crater edge lies is perpendicular to the 2D imaging plane of the camera. In this situation, the actual crater centre has the same line of sight direction as that of the crater centre. However, this situation is not the general case in practice. Figure 1 illustrates a more general landing scenario, where the line of sight of a crater centre in a descent image deviates from that of its counterpart in the crater map by $\delta\theta$.

Denote by r the radius of the actual crater's rim, and r_c the radius of the detected crater in a descent image. A numerical simulation is utilised to analyse the effect of the difference between the Lines-of-Sight (LoS) on lander pose estimation. In this simulation, a planetary lander is assumed to start crater-based navigation at altitude $50r$ and stop at altitude $5r$. Three globally referenced craters are utilised for examining the LoS bias and pose estimate error. The crater rims are assumed to lie in the same plane. In this simulation, the angle
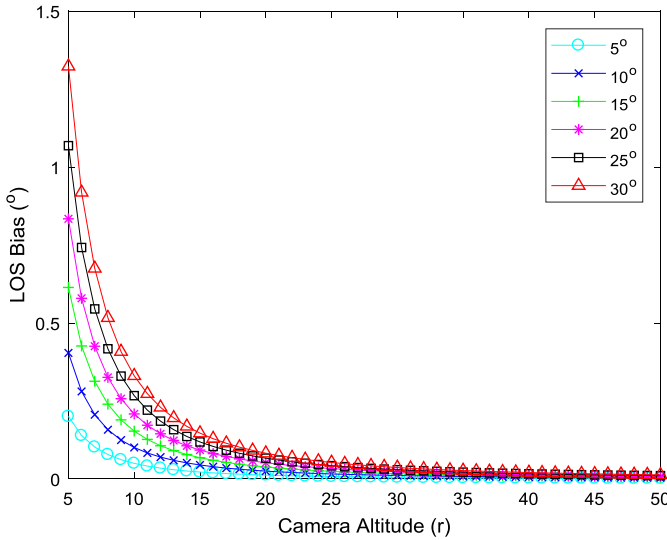
Figure 2.   Relationship between the LoS deviation and the camera altitude, given different angles of incidence.

of incidence between the camera optical axis and the crater plane is varied from 5° to 30° and the relationship between average LoS deviations and camera altitude is presented in Figure 2, wherein the camera altitude grows from 5r to 50r.

It can be seen from Figure 2 that the LoS deviation increases as the incident angle grows, and the LoS deviation also increases as camera altitude decreases.

Given three observed craters, the lander position is estimated via minimising the following cost function:

$$\mathcal{J}(\boldsymbol{P}) = \sum \left[\frac{(\boldsymbol{P} - \boldsymbol{L}_i)^T (\boldsymbol{P} - \boldsymbol{L}_j)}{\|(\boldsymbol{P} - \boldsymbol{L}_i)\| \|(\boldsymbol{P} - \boldsymbol{L}_j)\|} - \boldsymbol{v}_i^T \boldsymbol{v}_j \right]^2, \quad i,j = [1, 2, 3], \quad i \neq j \qquad (10)$$

where $\boldsymbol{P}$ is the lander's position, $\boldsymbol{L}_i$ and $\boldsymbol{L}_j$ are the location of the i-th and j-th crater, respectively; $\boldsymbol{v}_i$ and $\boldsymbol{v}_j$ are the LoS of the centre for the i-th and j-th crater, respectively.

Equation (10) aims at finding the best estimate of the lander's position by comparing three crater LoS with their counterparts in the database. Figure 3 presents the relationship between camera altitude and final positioning error. This shows that the position estimate error tends to increase as the camera altitude decreases. Figure 4 shows the relationship between the LoS deviation and position estimation error at different altitudes varying from 5r to 30r.

Figure 4 shows that the positioning error grows as the LoS deviation increases, which is to be expected, since a deviation of LoS also corresponds to the bias between the crater centre in the descent image and its counterpart in the navigation map. As a result, this bias will be propagated to the position estimation. For this reason, we propose to use the crater's edge instead of the crater centre to carry out the pose estimation, details of which are presented in the following sections.
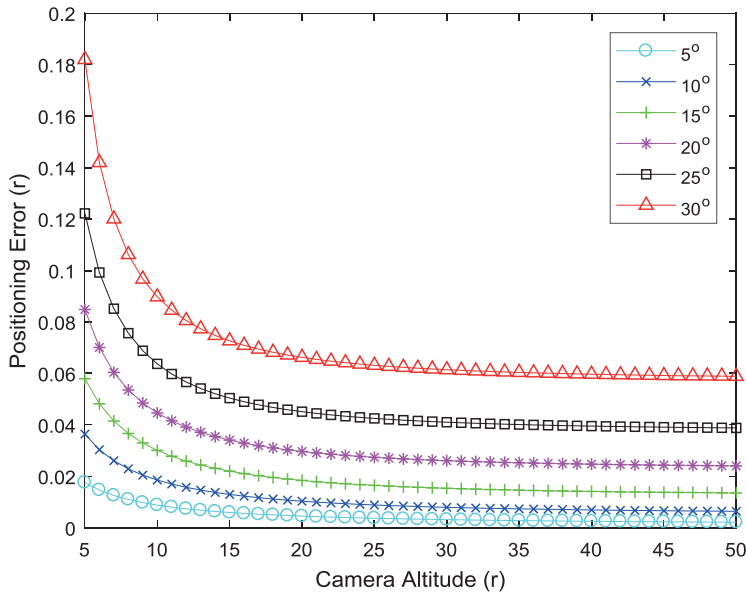
Figure 3.   Relationship between the camera altitude and position estimate error using three crater's LoS, given different angles of incidence.
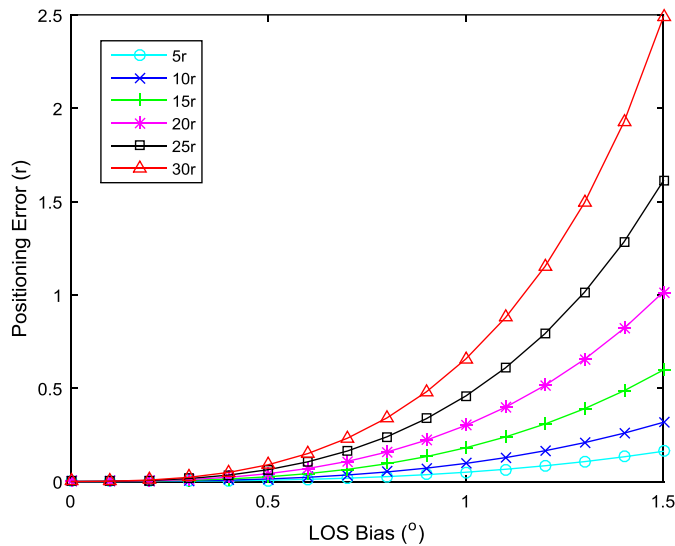

Figure 4.   Relationship between the LoS deviation and position estimate error at different altitudes.

3.   AUTONOMOUS NAVIGATION USING CRATER EDGE.   It is shown in Section 2 that solely using a crater centre as a navigation landmark introduces consistent position estimate errors. A crater edge, on the contrary, is relatively more robust against the variation of the observation's LoS. For this reason, a crater edge-based navigation solution is proposed in this Section.

It is assumed that the edges of craters are correctly detected by edge detection algorithms (for example, the Canny edge algorithm (Canny, 1986)), and a crater landmark database has been established, from which the 3D location, semi-major and semi-minor axes of craters can be readily obtained. To simplify the problem, it is assumed that the matrix that defines the rotation from the lander body frame to the camera's body frame is a pre-determined constant matrix. In what follows, three methods of using the crater edges for autonomous navigation are presented: the first method uses three or more craters, the second uses two craters and the third uses only one crater.

3.1. *Autonomous navigation based on three or more craters.* In this case, it is assumed that three or more craters are detected from a descent image and matched to craters in a globally referenced database. P is the pose of the lander, $i = 0, 1, \ldots, n$ is the corresponding crater's number; L_i is the location of the i-th crater edge curve in the celestial body fixed coordinate frame and n_i is the normal direction of its fitted plane. According to Equation (10), we have:

$$\frac{R_G^c(P - L_i)}{\|P - L_i\|} = \frac{K_i R_G^c n_i}{\|K_i R_G^c n_i\|} \tag{11}$$

where R_G^c is a matrix that defines the rotation from the camera body frame to the global frame (that is, the celestial body fixed coordinate frame) and the coefficient matrix K_i in Equation (11) is:

$$K_i = \begin{bmatrix} k_4 & k_5 & k_1 \\ k_5 & k_6 & k_2 \\ k_1 & k_2 & k_3 \end{bmatrix} \tag{12}$$

where $k_j, j = 1, 2, \ldots, 6$ corresponds to the same variable setup in Equations (8) and (9). It can be determined by fitting a representative ellipse to crater edges. According to Equation (11), a crater edge can yield two independent equations. When three or more craters are observed, the camera's six-Degree of Freedom (DoF) pose can be fully determined. Taking into account the observation noise and bias in crater edge fitting, the camera's position and attitude in the global frame can be solved via the following optimisation problem:

$$(P, R_G^c) = \arg\min_{P, R_G^c} \sum_{i=1,2,\ldots,n} \left\| \frac{R_G^c(P - L_i)}{\|P - L_i\|} - \frac{K_i R_G^c n_i}{\|K_i R_G^c n_i\|} \right\|^2 \tag{13}$$

3.2. *Autonomous navigation based on two craters.* The second scenario assumes that two craters are observed. Accordingly, four independent equations can be established by following Equation (11), however, they are not sufficient to solve a six-DoF camera pose. Thus, additional observation equations must be introduced. In doing so, the semi-major and semi-minor axes of the crater are employed as supplementary observations.

As shown in Figure 5, a local crater frame is constructed, wherein the semi-major and semi-minor axes of the crater are the x-axis and y-axis of this local frame, respectively; the z-axis is perpendicular to the crater's outer rim plane.
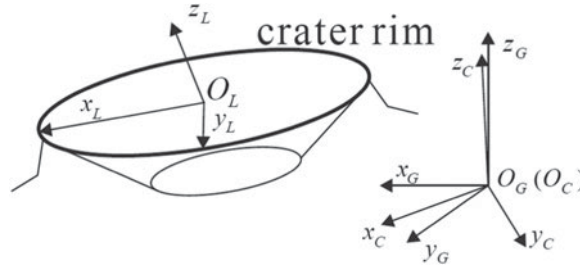
Figure 5.   Illustration of the local crater frame {L} and the global body fixe frame {G}.

Consider that all the crater edge curves are located in the XY plane of the {L} coordinate, the relationship between a 3D point on crater edge in the camera's body frame $X_C = [x_c, y_c, z_c]^T$ and its coordinate in the crater local frame $X_L = [x_L, y_L, x_L]^T$ can be denoted as:

$$\begin{bmatrix} x_c \\ y_c \\ z_c \end{bmatrix} = \boldsymbol{R}_L^c \begin{bmatrix} 1 & 0 & -t_x \\ 0 & 1 & -t_y \\ 0 & 0 & -t_z \end{bmatrix} \begin{bmatrix} x_L \\ y_L \\ z_L \end{bmatrix} = \boldsymbol{R}_L^c \boldsymbol{H} \begin{bmatrix} x_L \\ y_L \\ z_L \end{bmatrix} \tag{14}$$

where $\boldsymbol{T} = [t_x, t_y, t_z]^T$ is the position of the camera in the crater local frame, $\boldsymbol{R}_L^c$ is an attitude transition matrix that defines the rotation from the crater local frame {L} to the camera body frame {C}; $\boldsymbol{R}_c^G = \boldsymbol{R}_L^G \boldsymbol{R}_c^L$, where $\boldsymbol{R}_c^G$ is a matrix that defines the rotation from the crater local frame to the global frame, which can be found in previous investigations.

A representative ellipse in the crater local frame can be expressed as:

$$\begin{bmatrix} x_L \\ y_L \\ 1 \end{bmatrix}^T \underbrace{\begin{bmatrix} 1/a^2 & 0 & 0 \\ 0 & 1/b^2 & 0 \\ 0 & 0 & -1 \end{bmatrix}}_{\boldsymbol{C}} \begin{bmatrix} x_L \\ y_L \\ 1 \end{bmatrix} = 0 \tag{15}$$

where a and b are the length of the semi-major and semi-minor axes of a representative ellipse, respectively. Note that since $t_z > 0$, the transformation matrix $\boldsymbol{H}$ is invertible. Substituting Equation (14) into Equation (15) yields:

$$\boldsymbol{X}_c^T \boldsymbol{R}_L^c \boldsymbol{H}^{-T} \boldsymbol{C} \boldsymbol{H}^{-1} (\boldsymbol{R}_L^c)^T \boldsymbol{X}_c = \frac{1}{z_c^2} [u\ v\ 1] \boldsymbol{R}_L^c \boldsymbol{H}^{-T} \boldsymbol{C} \boldsymbol{H}^{-1} (\boldsymbol{R}_L^c)^T \begin{bmatrix} u \\ v \\ 1 \end{bmatrix} = 0 \tag{16}$$

Comparing Equation (16) with Equation (3), it can be seen that $\boldsymbol{H}^{-T} \boldsymbol{C} \boldsymbol{H}^{-1}$ can be related to $(\boldsymbol{R}_L^c)^T \boldsymbol{Q} \boldsymbol{R}_L^c$:

$$\alpha \boldsymbol{H}^{-T} \boldsymbol{C} \boldsymbol{H}^{-1} = (\boldsymbol{R}_L^c)^T \boldsymbol{Q} \boldsymbol{R}_L^c \tag{17}$$

where α is a scale factor, expanding Equation (17) yields:

$$
\begin{aligned}
\boldsymbol{r}_1^T \boldsymbol{Q} \boldsymbol{r}_1 &= \alpha/a^2 \\
\boldsymbol{r}_2^T \boldsymbol{Q} \boldsymbol{r}_2 &= \alpha/b^2 \\
\boldsymbol{r}_1^T \boldsymbol{Q} \boldsymbol{r}_2 &= 0 \\
\boldsymbol{r}_1^T \boldsymbol{Q} \boldsymbol{r}_3 &= -\alpha t_x/(a^2 t_z) \\
\boldsymbol{r}_2^T \boldsymbol{Q} \boldsymbol{r}_3 &= -a t_y/(b^2 t_z) \\
\boldsymbol{r}_3^T \boldsymbol{Q} \boldsymbol{r}_3 &= \frac{\alpha}{t_z^2}(t_x^2/a^2 + t_y^2/b^2 - 1)
\end{aligned}
\tag{18}
$$

where $\boldsymbol{r}_1$, $\boldsymbol{r}_2$, and $\boldsymbol{r}_3$ are three columns of $\boldsymbol{R}_L^c$, such that $\boldsymbol{R}_L^c = [\boldsymbol{r}_1 \; \boldsymbol{r}_2 \; \boldsymbol{r}_3]$. Eliminating the scaling factor α in Equation (18) yields:

$$
\boldsymbol{h}(\boldsymbol{R}_L^c, \boldsymbol{T}) =
\begin{bmatrix}
a^2 \boldsymbol{r}_1^T \boldsymbol{Q} \boldsymbol{r}_1 - b^2 \boldsymbol{r}_2^T \boldsymbol{Q} \boldsymbol{r}_2 \\
\boldsymbol{r}_1^T \boldsymbol{Q} \boldsymbol{r}_2 \\
t_z \boldsymbol{r}_1^T \boldsymbol{Q} \boldsymbol{r}_3 + t_x \boldsymbol{r}_1^T \boldsymbol{Q} \boldsymbol{r}_1 \\
t_z \boldsymbol{r}_2^T \boldsymbol{Q} \boldsymbol{r}_3 + t_y \boldsymbol{r}_2^T \boldsymbol{Q} \boldsymbol{r}_2 \\
(a^2 - t_x^2) \boldsymbol{r}_1^T \boldsymbol{Q} \boldsymbol{r}_1 - t_y^2 \boldsymbol{r}_2^T \boldsymbol{Q} \boldsymbol{r}_2 + t_z^2 \boldsymbol{r}_3^T \boldsymbol{Q} \boldsymbol{r}_3
\end{bmatrix}
= \boldsymbol{0}_{5 \times 1}
\tag{19}
$$

According to the definition of $\boldsymbol{K}$ and $\boldsymbol{Q}$, $\boldsymbol{K}$ can be related to $\boldsymbol{Q}$ by noting that:

$$
\boldsymbol{K}^{-1} = \boldsymbol{Q}/(B^2 - 4AC)F + CD^2 - BDE + AE^2
\tag{20}
$$

Considering $\boldsymbol{R}_G^L(\boldsymbol{P} - \boldsymbol{L}) = \boldsymbol{T}$ and $\boldsymbol{R}_G^L \boldsymbol{n} = [0 \; 0 \; 1]^T$, and multiplying Equation (11) by $(\boldsymbol{R}_L^c)^T \boldsymbol{Q}$:

$$
\frac{(\boldsymbol{R}_L^c)^T \boldsymbol{Q} \boldsymbol{R}_L^c \boldsymbol{T}}{\|(\boldsymbol{R}_L^c)^T \boldsymbol{Q} \boldsymbol{R}_L^c \boldsymbol{T}\|} = [0 \; 0 \; 1]^T
\tag{21}
$$

which can also be expressed by two independent equations:

$$
\begin{aligned}
t_x \boldsymbol{r}_1^T \boldsymbol{Q} \boldsymbol{r}_1 + t_y \boldsymbol{r}_1^T \boldsymbol{Q} \boldsymbol{r}_2 + t_z \boldsymbol{r}_1^T \boldsymbol{Q} \boldsymbol{r}_3 &= 0 \\
t_x \boldsymbol{r}_1^T \boldsymbol{Q} \boldsymbol{r}_2 + t_y \boldsymbol{r}_2^T \boldsymbol{Q} \boldsymbol{r}_2 + t_z \boldsymbol{r}_2^T \boldsymbol{Q} \boldsymbol{r}_3 &= 0
\end{aligned}
\tag{22}
$$

Equation (22) can also be derived from the second, third and fourth equations of Equation (19). When two craters are observed, the first and second equations in Equation (19) and Equation (11) can be employed to estimate the camera pose:

$$
(\boldsymbol{P}, \boldsymbol{R}_G^c) = \arg \min_{\boldsymbol{P}, \boldsymbol{R}_G^c} \left(\sum_{i=1,2} \left\{ \left\| \frac{\boldsymbol{R}_G^c(\boldsymbol{P} - \boldsymbol{L}_i)}{\|\boldsymbol{P} - \boldsymbol{L}_i\|} - \frac{\boldsymbol{K}_i \boldsymbol{R}_G^c \boldsymbol{n}_i}{\|\boldsymbol{K}_i \boldsymbol{R}_G^c \boldsymbol{n}_i\|} \right\|^2 \right. \right.
$$
$$
\left. \left. + \left(a_i^2 \boldsymbol{r}_1^{i^T} \boldsymbol{Q}_i \boldsymbol{r}_1^i - b_i^2 \boldsymbol{r}_2^{i^T} \boldsymbol{Q}_i \boldsymbol{r}_2^i \right)^2 + (\boldsymbol{r}_1^{i^T} \boldsymbol{Q}_i \boldsymbol{r}_2^i)^2 \right\} \right)
\tag{23}
$$

where the first term corresponds to the deviation of normals of the rim plane; the second term corresponds to the deviation of crater edges.
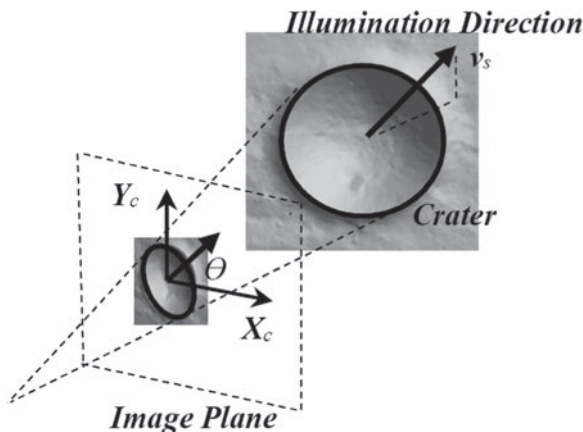
Figure 6.   Schematic of using the solar Illumination Direction as a complementary observation.

3.3.   *Autonomous navigation based on a single crater.*   When only one crater is observed, Equation (19) is no longer valid, thus more observations must be introduced. In doing so, it is proposed to use the solar illumination direction as a complementary observation, an illustrative example is shown in Figure 6.

The solar illumination direction can be estimated by the grayscale or first-order derivative of the greyscale of pixels from a descent image (Pentland, 1984). As is shown in Figure 6, denote by $v_s = [v_s^x \ v_s^y \ v_s^z]^T$ the solar illumination angle, θ the tilt angle of the illumination direction in a descent image and θ is related to v_s by:

$$h_s(\boldsymbol{R}_G^c) = \theta - \tan^{-1}\left(\frac{r_{21}v_s^x + r_{22}v_s^y + r_{23}v_s^z}{r_{11}v_s^x + r_{12}v_s^y + r_{13}v_s^z}\right) = 0 \qquad (24)$$

where r_{ij} is the element in the i-th row and j-th column of the attitude matrix $\boldsymbol{R}_G^c$ and v_s is assumed as an *a-priori* known value throughout the landing process. Therefore, Equation (24) can be employed to estimate the tilt angle of solar illumination direction, which is then used as a supplementary observation, such that:

$$\boldsymbol{h}_{total}(\boldsymbol{R}_G^c, \boldsymbol{P}) = \begin{bmatrix} \boldsymbol{h}(\boldsymbol{R}_G^c \boldsymbol{R}_L^G, \boldsymbol{R}_G^L(\boldsymbol{P} - \boldsymbol{L})) \\ h_s(\boldsymbol{R}_G^c) \end{bmatrix} = \begin{bmatrix} \boldsymbol{h}(\boldsymbol{R}_L^c, \boldsymbol{T}) \\ h_s(\boldsymbol{R}_G^c) \end{bmatrix} = \boldsymbol{0}_{6\times 1} \qquad (25)$$

Using Equation (25) as the observation model, the Extended Kalman Filter (EKF) can be employed to carry out pose estimation. It should be noted that the observation model is a function of crater edge coefficients $q = [A, B, C, D, E, F]^T$ and tilt angle of solar illumination direction θ. As a result, the EKF must use the implicit observation models introduced by Soatto et al. (1996). The lander state evolution model can be formulated by:

$$\ddot{\boldsymbol{P}} = \boldsymbol{R}_c^b \boldsymbol{a}_c + \boldsymbol{U} - 2\boldsymbol{\omega} \times \dot{\boldsymbol{P}} - \boldsymbol{\omega} \times (\boldsymbol{\omega} \times \boldsymbol{P}) \qquad (26)$$

$$\dot{\boldsymbol{q}} = \frac{1}{2}\boldsymbol{\Omega}(\boldsymbol{\omega}_b - \boldsymbol{\omega})\boldsymbol{q} \qquad (27)$$

where the lander state $[\boldsymbol{P}, \boldsymbol{q}]^T$ is characterised in the lander body-fixed frame; $\boldsymbol{U}$ is the gravitational acceleration of the target planet; $\boldsymbol{\omega}$ is the spin angular velocity of the target
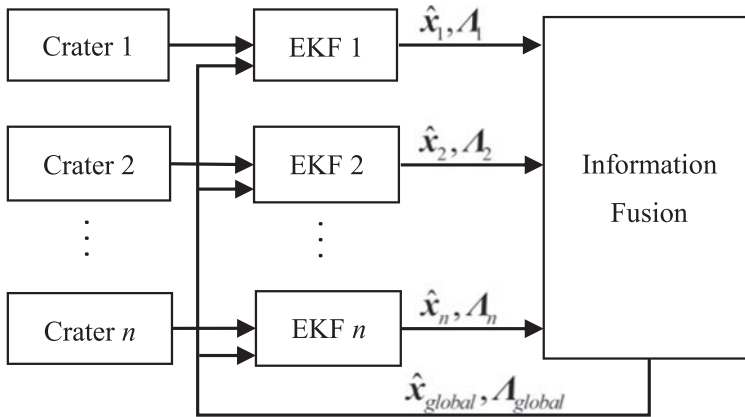
Figure 7.   Structure of distributed EKF filter based on crater edges.

planet; $\boldsymbol{a}_c$ is the thrust control; $\boldsymbol{R}_c^b$ is a matrix that defines the rotation from the thruster installation frame to the body frame; $\boldsymbol{q}$ is the lander attitude expressed by quaternion, $\boldsymbol{\omega}_b$ is the angular velocity of the lander, and $\boldsymbol{\Omega}(\boldsymbol{\omega})$ is defined to be:

$$\boldsymbol{\Omega}(\boldsymbol{\omega}) = \begin{bmatrix} 0 & -\omega_x & -\omega_y & -\omega_z \\ \omega_x & 0 & \omega_z & -\omega_y \\ \omega_y & -\omega_z & 0 & \omega_x \\ \omega_z & \omega_y & -\omega_x & 0 \end{bmatrix} \tag{28}$$

where ω_x, ω_y and ω_z are three elements of $\boldsymbol{\omega}$. An Inertial Measurement Unit (IMU) can be employed to provide high update frequency measurements of angular velocity and acceleration, that is, $\boldsymbol{\omega}_b$ and $\boldsymbol{R}_c^b \boldsymbol{a}_c$. Following the state evolving Equations (26) and (27), the single-crater based observation model can be readily introduced in the state update step of the EKF to complete a crater-aided inertial navigation filter.

The single crater-based method can be easily extended to the case of multiple craters. In doing so, a distributed lander state estimation method is constructed to include these three aforementioned methods, Figure 7 illustrates the basic outline of this distributed EKF filter. The main idea is to establish an EKF for each observed crater. Denote by $\hat{\boldsymbol{x}}_i$ and $\boldsymbol{\Lambda}_i$ the lander state estimation and covariance for the i-th EKF, respectively. If more than one crater is observed, according to the principle of information fusion, the lander state and covariance can be given by:

$$\hat{\boldsymbol{x}}_{global} = \boldsymbol{\Lambda}_{global} \sum_{i=1}^{n} \boldsymbol{\Lambda}_i^{-1} \hat{\boldsymbol{x}}_i$$

$$\boldsymbol{\Lambda}_{global} = \left(\sum_{i=1}^{n} \boldsymbol{\Lambda}_i^{-1} \right)^{-1} \tag{29}$$

where $\hat{\boldsymbol{x}}_{global}$ and $\boldsymbol{\Lambda}_{global}$ are the final state estimation and covariance. This distributed estimation method simplifies the design of the navigation filter. In the meantime, its observation model works in an augmented manner, such that any new observed craters can be readily incorporated into the navigation filter.

4. SIMULATION RESULTS AND DISCUSSION.

4.1. *Crater detection and ellipse fitting validation.* Some craters are not naturally elliptically-shaped. To investigate the effect of shape deformation on the performance of crater detection, a simulation using real planetary images was carried out. A crater map of Dione from its 3D shape model was established (Gaskell, 2013), in which 3D crater models are globally referenced. An overview of the Dione shape model along with some parts of the crater map is shown in Figure 8. Orbital images acquired from the *Cassini* mission were employed as a test bed, to which the crater detection algorithm proposed by Yu et al. (2014) was applied.

For each orbital image, crater models were projected onto the image using the true camera pose to yield true crater parameters, which were compared with the parameters of detected craters to determine the ellipse fitting error in crater detection.

The overall crater detection rate is 92%, which is consistent with state-of-the-art crater detection studies (Yu et al., 2014; Cheng et al., 2005; Woicke et al., 2018). The detected craters were classified into two groups, namely the fine shape group and the irregular group. Table 1 shows the ellipse fitting error results (unit: pixel), where the crater centre position bias, semi-major and semi-minor axis length bias between detected craters and their counterparts in the crater map are calculated.

From Table 1 it can be seen that the ellipse fitting method for the fine-shape group yields an average bias of less than one pixel for three parameters, indicating a plausible ellipse fitting result. In comparison, the parameter biases in the irregular shape group are roughly three times bigger than those in the fine shape group. An important lesson was learned from this simulation, which is that the shape of the crater has an effect on navigation accuracy. To cope with this issue, one possible solution is to remove the craters with irregular shapes
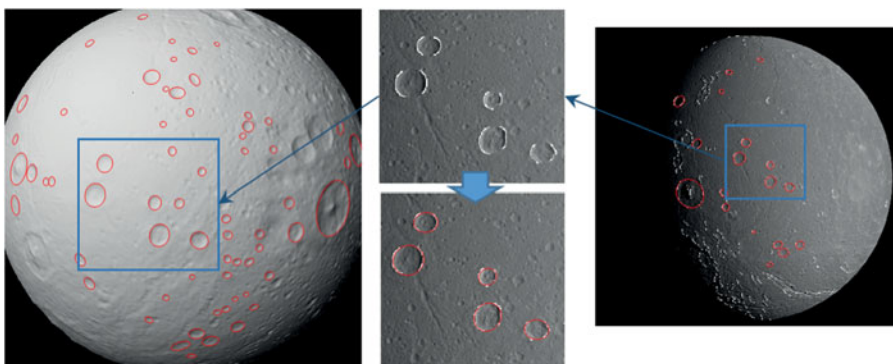

Figure 8. Crater map of Dione (Moon of Saturn) along with demonstrations of crater detection and ellipse fitting.

Table 1. Average fitting errors of crater rims (unit: pixel).

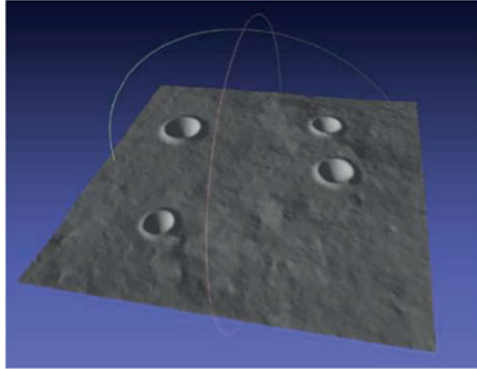|	Crater's centre position bias	semi-major axis bias	semi-minor axis bias
Average value (fine shape)	0.4925	0.4338	0.5083
Maximum value (fine shape)	2.0031	1.8743	1.5783
Average value (irregular shape)	1.5421	1.3123	1.7831
Maximum value (irregular shape)	5.3221	4.2032	4.0923

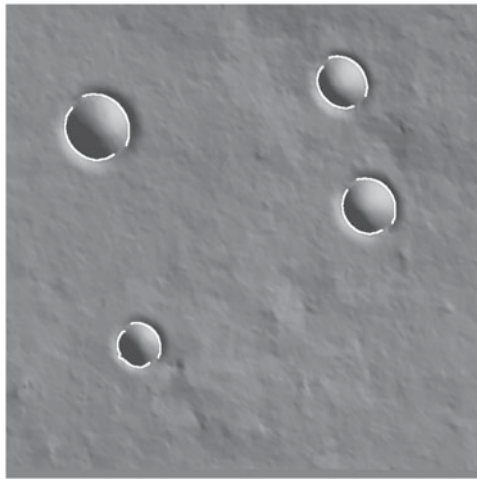Figure 9.   Overview of a 3D terrain.

Figure 10.   Generated image and edge detection results.

from the crater map, thereby guiding the crater matching to be carried out between craters with regular shapes.

4.2.   *Simulation of crater-based navigation method.*   A terrain landscape simulator was developed as a test bed for validating the proposed algorithm. An example of the simulated 3D terrain is presented in Figure 9; this simulator can generate craters with arbitrary size and shape. In this example case, four craters with different size and location were simulated. The Canny edge algorithm (Canny, 1986) was adopted to detect the crater's edge, Figure 10 shows the rendered descent image of Figure 9 along with the crater edge detection results. The resolution of a rendered image was set to 1024×1024, and the field of view of the navigation camera was set to $44° \times 44°$.

4.2.1.   *Case one: Three or more craters.*   The first simulation was carried under the condition where three or more craters were observed. Three non-overlapping crater edge curves were randomly generated in the field of view of the on board camera, the length of the semi-major and semi-minor axes were randomly selected in the range 0.5 km–2.5 km,
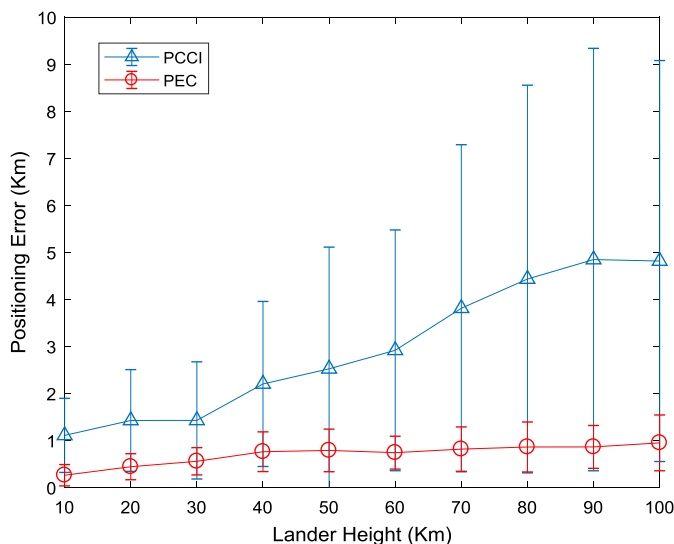
Figure 11. Means and standard deviations of position estimate error under the condition of three or more craters observed.

and the maximum angle between the crater normal and the optical axis of the camera was set to $30°$. The length of the crater edge was randomly selected to be in the range $10 \sim 100$ pixels. Points on the crater edge had Gaussian-distributed noise added with a standard deviation of one pixel. The altitude of the lander varied between 10 km–100 km. At each altitude, a hundred Monte Carlo simulations were carried out using the proposed method. The means and standard deviation of position estimate error are presented in Figure 11.

As shown in Figure 11, the average positioning error and its standard deviation error tend to grow as the altitude of the lander increases, the minimum position estimate error is $0·258$ km $\pm 0·227$ km, which occurs at an altitude of 10 km; the maximum position estimate error is $0·945$ km $\pm 0·593$ km, which occurs at an altitude of 100 km. The trend of position estimate error using the Positioning method of the Crater Image Centre (PCCI) is the same as Positioning method based on the Edge of Crater (PEC), but the average position estimate error and the corresponding standard deviation are significantly higher than that with the PEC method. Simulation results indicate that when the optical axis of the navigation camera is not parallel to the normal of the crater, the deviation between the centre of the crater in the descent image and its true line of sight has a non-negligible effect on the pose estimation. Figure 12 shows the means and standard deviations of attitude estimate error results. Unlike the position estimation results, the overall trend of the attitude estimate error decreases as the altitude increases.

4.2.2. *Case two: Two craters.* The same simulation conditions were applied to the case where two craters were observed. The position and attitude error are shown in Figures 13 and 14, respectively.

As shown in Figures 13 and 14, the maximum average position estimate error is $0·107$ km at altitude 100 km with a standard deviation of $0·203$ km; the maximum average attitude estimate error is $0·173°$ at altitude 80 km with a standard deviation of $0·35°$. The error of position estimate using two craters was even smaller than using three or more
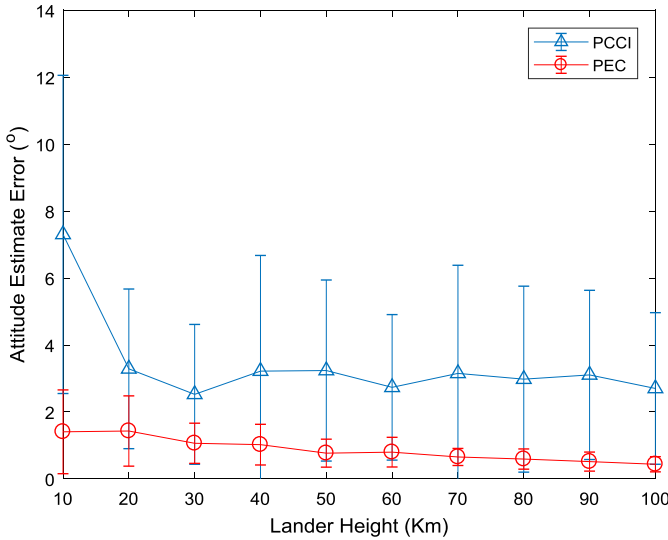
Figure 12.   Means and standard deviations of attitude estimate error under the condition of three or more craters observed.
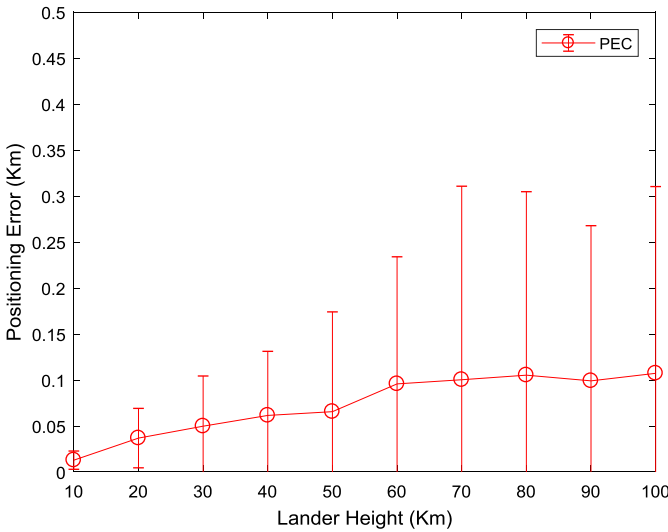

Figure 13.   Average positioning error and standard deviation of error with two craters.

crater centres (PCCI method), which is mainly due to imposed constraints of the crater shape parameters.

4.2.3. *Case three: Single/multiple craters and distributed EKF filter.*   Finally, the single crater-based navigation method along with other proposed methods was verified under the distributed EKF filter structure. Consider that the proposed method relies on the elliptical parameters of the detected edge (see Equation (3), parameters A~F), the standard deviations (std.) of the estimated error of the edge parameters is presented in Table 2. The
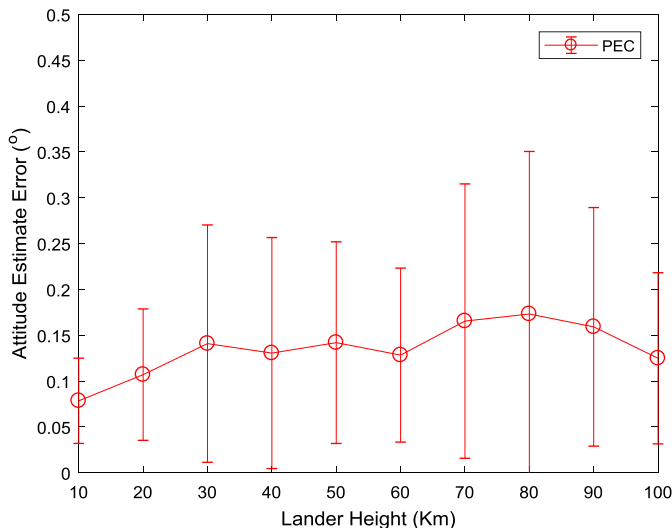
Figure 14. Average attitude error and standard deviation of error with two craters.

Table 2. Standard deviation of error in crater edge parameter estimation at different altitudes.

| Altitude (Km) | Standard deviation of error in crater edge parameter estimation | | | | | |
	A	B	C	D	E	F
50	$1 \cdot 26 \times 10^{-6}$	$1 \cdot 98 \times 10^{-5}$	$3 \cdot 06 \times 10^{-6}$	$2 \cdot 40 \times 10^{-4}$	$2 \cdot 25 \times 10^{-4}$	$2 \cdot 91 \times 10^{-6}$
40	$1 \cdot 68 \times 10^{-3}$	$7 \cdot 61 \times 10^{-3}$	$1 \cdot 04 \times 10^{-3}$	$3 \cdot 67 \times 10^{-4}$	$4 \cdot 03 \times 10^{-4}$	$1 \cdot 42 \times 10^{-5}$
30	$2 \cdot 45 \times 10^{-3}$	$7 \cdot 42 \times 10^{-3}$	$1 \cdot 30 \times 10^{-3}$	$1 \cdot 63 \times 10^{-4}$	$1 \cdot 85 \times 10^{-4}$	$7 \cdot 78 \times 10^{-6}$
20	$2 \cdot 44 \times 10^{-3}$	$8 \cdot 59 \times 10^{-3}$	$2 \cdot 60 \times 10^{-3}$	$3 \cdot 00 \times 10^{-4}$	$3 \cdot 06 \times 10^{-4}$	$1 \cdot 78 \times 10^{-5}$
10	$3 \cdot 08 \times 10^{-3}$	$8 \cdot 00 \times 10^{-3}$	$3 \cdot 06 \times 10^{-3}$	$6 \cdot 28 \times 10^{-4}$	$6 \cdot 41 \times 10^{-4}$	$7 \cdot 98 \times 10^{-5}$

std. errors were collected by extracting crater edges from several rendered descent images. Specifically, for each altitude, 128 rendered images were first used to detect the crater edges, and then the edge curve parameters' errors were collected.

Results from Table 2 can serve as a reference to set the observation noise. Accordingly, the covariance of the measurement noise in the distributed EKF filter was set to:

$$Q_n = \begin{bmatrix} 2 \cdot 5 \times 10^{-5} & 0 & 0 & 0 & 0 & 0 \\ 0 & 1 \cdot 5 \times 10^{-4} & 0 & 0 & 0 & 0 \\ 0 & 0 & 2 \cdot 5 \times 10^{-5} & 0 & 0 & 0 \\ 0 & 0 & 0 & 1 \cdot 5 \times 10^{-6} & 0 & 0 \\ 0 & 0 & 0 & 0 & 1 \cdot 5 \times 10^{-6} & 0 \\ 0 & 0 & 0 & 0 & 0 & 1 \cdot 5 \times 10^{-8} \end{bmatrix}$$

A sub-EKF was constructed for each crater after obtaining its edge parameters A~F. The filter state includes the lander's three-axis position, velocity, angular velocity and lander attitude expressed by quaternions. If multiple craters were observed, the information was fused to couple all the sub-EKFs into a distributed EKF filter, which corresponds to Equations (25)~(29).
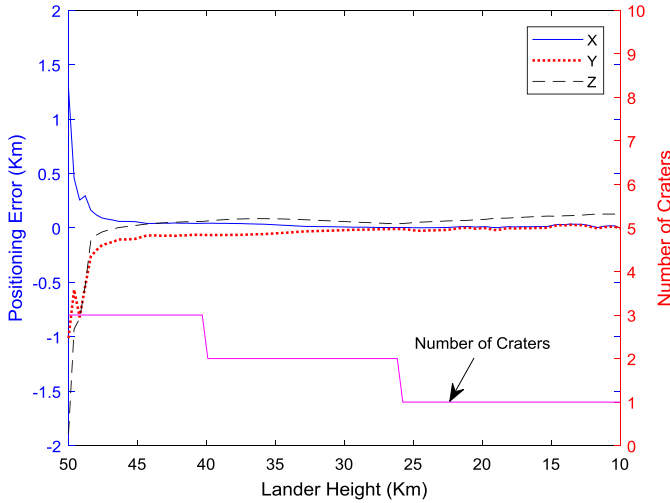
Figure 15.   Position estimate error of the crater edge-based distributed EKF filter.
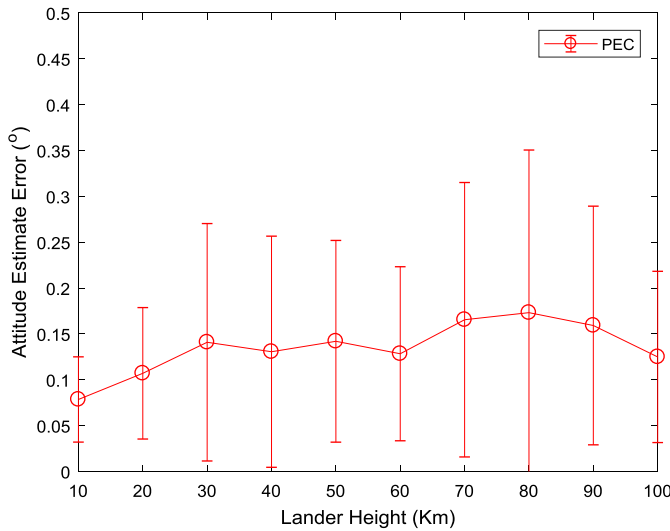

Figure 16.   Attitude estimate error of the crater edge-based distributed EKF filter.

The same simulation parameter set-up in the first and second case was followed. To simplify the problem, the attitude of the lander was assumed to remain stable throughout the descent. Figures 15 and 16 show the time history of the lander pose estimation error along with the number of observed craters for one simulation trial. During the initial phase of the descent, the number of observed craters was three. The position and attitude errors of the lander quickly converged to 40 m and 0.05° at an altitude of 26 km. After the lander reached 26 km, the on board camera can only observe one crater, causing the attitude estimation error to slightly increase as the landing proceeds. This is because the solar illumination direction, as a complementary observation to estimate the lander's pose, is much
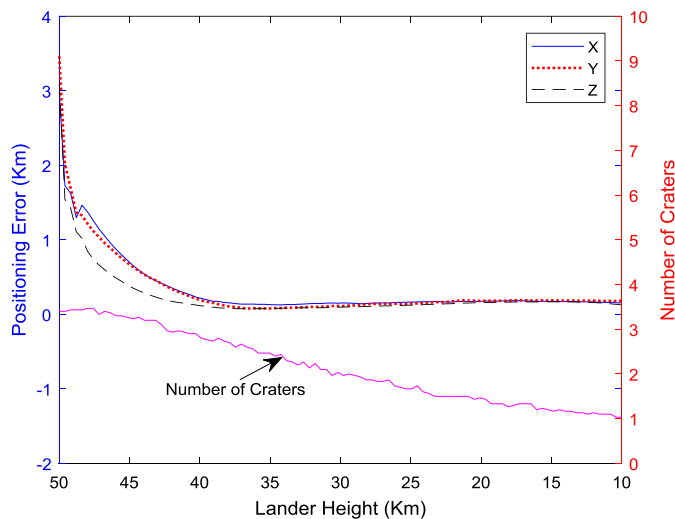
Figure 17.   Average lander position estimated error of the MC simulation.
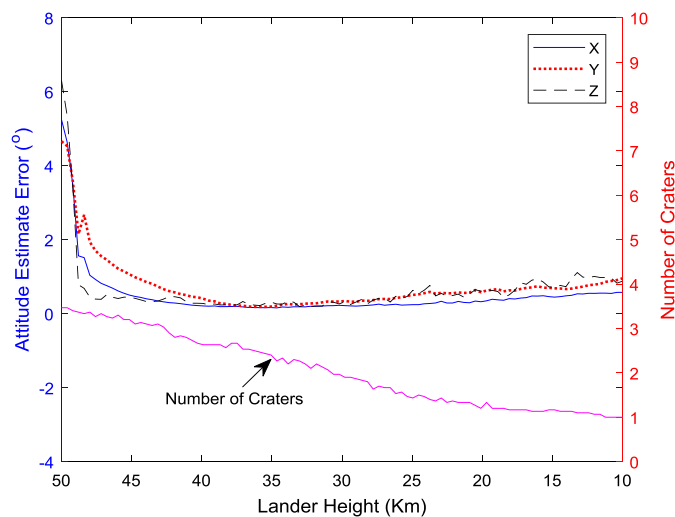

Figure 18.   Average lander attitude estimated error of the MC simulation.

less accurate than the crater edge estimation. Nevertheless, the crater edge-based navigation method is still effective in suppressing the accumulated errors.

A total number of thirty sets of simulated terrains were generated for the Monte Carlo (MC) simulation. In each MC trial, the initial lander position, velocity, attitude and angular velocity were assumed to be mixed with zero-mean Gaussian distributed noise, with standard deviations of 4 km, 5 m/s, 25 deg and 5°/s, respectively. The standard deviation of the tilt angle noise for the solar illumination direction is 10°. Figures 17 and 18 show the average position and attitude estimate error collected from the MC simulation. Along with the estimated error, the average number of craters which lie in the camera's field of view

is shown in these two figures. It can be seen that the average position and attitude estimation tend to converge when at least two craters are observed. When the average number of observed craters is less than two, the pose estimated error grows slowly as the landing proceeds. When the lander reaches the final recorded altitude at 10 km, the average position estimate error is less than 200 m, and the average attitude estimate error is less than $1°$, demonstrating the effectiveness of the proposed crater edge-based navigation approach.

5. CONCLUSION.   This paper presents a novel method for autonomous navigation during an extra-terrestrial body landing mission. The proposed method establishes crater edge and solar illumination direction-based measurement models and incorporates the measurement models into a distributed EKF filter to achieve crater-aided inertial navigation. Monte Carlo Simulations show that the proposed approach performs better than the state-of-the-art crater centre-based algorithms and is able to give a plausible estimate result when only one crater is observed, demonstrating its superiority in terms of navigation flexibility.

Future work will include a more credible semi-physical test of the proposed algorithm, where the effect of lighting conditions, crater shape, and other factors on navigational performance will be investigated.

REFERENCES

Ansar, A. (2004). small body GN&C research report: Feature recognition algorithms. *In Small Body Guidance Navigation and Control FY 2004 RTD Annual Report, Pasadena, CA.*

Bandeira, L., Saraiva, J. and Pina, P. (2007). Impact crater recognition on Mars based on a probability volume created by template matching. *IEEE Transactions on Geoscience and Remote Sensing*, **45**, 4008–4015.

Berry, K., Sutter, B., May, A., Williams, K., Barbee, B. W., Beckman, M. and Williams, B. (2013). OSIRIS-REx Touch-And-Go (TAG) mission design and analysis. *36th Annual AAS Guidance and Control Conference, Breckenridge, CO*, 667–678, 1–6 February.

Canny, J. (1986). A computational approach to edge detection. *IEEE Transactions on Pattern Analysis and Machine Intelligence*, **6** (1986), 679–698.

Cheng, Y., Johnson, A. E., Matthies, L. H. and Olson, C. F. (2003). Optical landmark detection for spacecraft navigation. *AAS/AIAA Astrodynamics Specialist Conference, Ponce, Puerto Rico*, pp: 1767–1785.

Cheng, Y. and Ansar, A. (2005). Landmark based position estimation for pinpoint landing on Mars. *Proceedings of the 2005 IEEE International Conference on Robotics and Automation, Barcelona, Spain*, pp: 4470–4475, 18–22 April.

Cheng, Y., Johnson, A. E. and Matthies, L. (2005). MER-DIMES: a planetary landing application of computer vision. *IEEE Computer Society International Conference on Computer Vision and Pattern Recognition, San Diego, CA*, pp: 806–813.

Gaskell, R. W. (2001). Automated landmark identification for spacecraft navigation. *2001 AAS/AIAA Astrodynamic Specialist Conference, Quebec City, Quebec, Canada*, pp: 1749–1756.

Gaskell, R.W. (2013). Gaskell Dione Shape Model V1.0. CO-SA-ISSNA/ISSWA-5-DIONESHAPE-V1.0. *NASA Planetary Data System.*

Johnson, A. E. (2000). Surface landmark selection and matching in natural terrain. *Proceedings of the IEEE Conference on Computer Vision and Pattern Recognition, Hilton Head Island, SC, USA*, pp: 413–420, 13–15 June.

Johnson, A. E. and SanMartin, A. M. (2000). Motion estimation from laser ranging for autonomous comet landing. *IEEE International Conference on Robotics and Automation, San Francisco, CA, USA*, pp: 132–138, 24–28 April.

Johnson, A. E., Willson, R., Cheng, Y., Goguen, J., Leger, C., SanMartin, M. and Matthies, L. (2007). Design through operation of an image-based velocity estimation system for Mars landing. *International Journal of Computer Vision*, **74**, 319–341.

Johnson, A. E. and Montgomery, J. F. (2008). Overview of terrain relative navigation approaches for precise Lunar landing. *IEEE Aerospace Conference, Big Sky, MT, USA*, pp: 1–10, 1–8 March.

Johnson, A. E., Cheng, Y., Montgomery, J. F., Trawny, N., Tweddle, B. and Zheng, J. X. (2015). Real-time terrain relative navigation test results from a relevant environment for Mars landing. *AIAA Guidance Navigation and Control Conference, Kissimmee, Florida, USA*, 5–9 January.

Leroy, B., Medioni, G., Johnson, A. E. and Matthies, L. H. (2001). Crater detection for autonomous landing on asteroids. *Image and Vision Computing*, **19**, 787–792.

Lorenz, A., Olds, R., May, A., Mario, C., Perry, M. E., Palmer, E. E. and Daly, M. (2017). Lessons learned from OSIRIS-Rex autonomous navigation using natural feature tracking. *IEEE Aerospace Conference, Big Sky, MT, USA*, pp: 1–12, 4–11 March.

Montgomery, J., Johnson, A. E., Roumeliotis, S. and Matthies, L. (2006). The JPL Autonomous Helicopter Testbed: A Platform for Planetary Exploration Technology Research and Development. *Journal of Field Robotics*, Special Issue on UAV's, 23.

Mourikis, A. I., Trawny, N., Roumeliotis, S. I., Johnson, A. E., Ansar, A. and Matthies, L. (2009). Vision-aided inertial navigation for spacecraft entry, descent, and landing. *IEEE Transactions on Robotics*, **25**, 264–280.

Pardo de Santayana, R. and Lauer, M. (2015). Optical measurements for Rosetta navigation near the Comet. *Proceedings of the 25th International Symposium on Space Flight Dynamics, Munich, Germany,* pp: 1–19.

Pentland, A. P. (1984). Local shading analysis. *IEEE Transactions on Pattern Analysis and Machine Intelligence*, **6**, 170–187.

Rohrschneider, R. (2011). Terrain relative navigation using crater identification in surface topography data. *AIAA Guidance, Navigation, and Control Conference, Portland, Oregon*, 8–11 August.

Simard Bilodeau, V., Neveu, D., Bruneau-Dbuc, S., Alger, M., LaFontaine, J. de, Clerc, S. and Drai, R. (2012). Pinpoint Lunar landing navigation using crater detection and matching: design and laboratory validation. *AIAA Guidance Navigation and Control Conference, Minneapolis, Minnesota*, 13–16 August.

Singh, L. and Lim S. (2008). On Lunar on-orbit vision-based navigation: terrain mapping, feature tracking driven EKF. *AIAA Guidance, Navigation and Control Conference and Exhibit, Honolulu, Hawaii*, 18–21 August.

Soatto, S., Frezza, R. and Perona, P. (1996). Motion estimation via dynamic vision. *IEEE Transactions on Automatic Control*, **41**, 393–413.

Spigai, M., Clerc, S. and Simard Bilodeau, V. (2010). An image segmentation-based crater detection and identification algorithm for planetary navigation. *Intelligent Autonomous Vehicles, Lecce, Italy*, 6–8 September.

Terui, F., Ogawa, N., Oda, K. and Uo, M. (2010). Image based navigation and guidance for approach and touchdown phase to an asteroid utilizing captured images at the rehearsal operation. *The 61st International Astronautical Congress, Prague, Czech Republic*, pp: 5963–5970.

Woicke, S., Moreno Gonzalez, A. S., El-Hajj, I., Mes, J. W. F., Henkel, M., Autar, R. and Klavers, R. (2018). Comparison of crater-detection algorithms for terrain-relative navigation. *2018 AIAA Guidance Navigation and Control Conference, Kissimmee, Florida, USA*, 8–12 January.

Yu, M., Cui, H. and Tian, Y. (2014). A new approach based on crater detection and matching for visual navigation in planetary landing. *Advances in Space Research*, **53**, 1810–1821.